Electronic Supplementary Information

A one-stone-two-birds strategy to construct metal-organic framework-derived cobalt phosphide as an efficient bifunctional electrocatalyst for oxygen electrode reactions

Hao Pan, Xiao-Li Wang,* Fayan Li and Qiang Xu*

Shenzhen Key Laboratory of Micro/Nano-Porous Functional Materials (SKLPM), SUSTech-Kyoto University Advanced Energy Materials Joint Innovation Laboratory (SKAEM-JIL), Key University Laboratory of Highly Efficient Utilization of Solar Energy and Sustainable, Development of Guangdong, Department of Materials Science and Engineering and Department of Chemistry, SUSTech Academy for Advanced Interdisciplinary Studies, Southern University of Science and Technology (SUSTech), Shenzhen 518055, China.

E-mail addresses:

wangxl7@sustech.edu.cn (X.-L. Wang),

xuq@sustech.edu.cn (Q. Xu)

Experimental Section

Chemicals and Reagents

All the chemicals were purchased and used without further purification. Zinc nitrate hexahydrate ($Zn(NO_3)_2 \cdot 6H_2O$, ≥99.00%), cobalt nitrate hexahydrate ($Co(NO_3)_2 \cdot 6H_2O$, ≥99.00%), 2-methylimidazole (2-MIM, ≥98.00%), zinc acetate dihydrate ($Zn(OAc)_2 \cdot 2H_2O$, ≥99.00%), cobalt(II) acetate tetrahydrate ($Co(OAc)_2 \cdot 4H_2O$, ≥99.50%), potassium hydroxide (KOH, ≥85.00%), 5.00% nafion solution, acrylamide (AM, ≥99.00%), N,N′-Methylenebis(acrylamide), potassium persulfate ($K_2S_2O_8$, ≥99.99%) and dimethyl sulfoxide (DMSO, ≥99.00%) were purchased from Aladdin Industrial Corporation. Phytic acid solution ($C_6H_{18}O_{24}P_6$) was purchased from Sinopharm Chemical Reagent Co., Ltd. Commercial Pt/C (20 wt%) catalyst was purchased from Sigma-Aldrich. Commercial RuO_2 catalyst and polytetrafluoroethylene (PTFE) preparation (60 wt%) was purchased from Macklin.

Material Synthesis

Synthesis of ZIF-L

For the synthesis of ZIF-L, two solutions were prepared by dissolving 2.0 mmol $Zn(NO_3)_2 \cdot 6H_2O$ and 0.4 mmol $Co(NO_3)_2 \cdot 6H_2O$ (Zn/Co = 5:1) in 40 mL deionized water (DI water) and 8.0 mmol 2-MIM in 40 mL DI water, respectively. Then, the ligand solution was poured into the solution of metal salt, followed by stirring at room temperature for 4 h. Finally, the obtained purple ZIF-L was collected by centrifugation, washed with DI water and ethanol, and dried.

Synthesis of ZIF-L@M-PA

First, 0.24 g ZIF-L was dispersed into water/ethanol mix solution (40 mL DI water and 4mL ethanol) and stirred at room temperature to form mixed solution. Then, 40 mL phytic acid solution ($V_{\text{phytic acid}}$: $V_{\text{DI water}}$ = 1:500) was added to the solution of ZIF-L. Afterwards, the mixture solution was stirred at room temperature for 30 min. Finally, ZIF-L@M-PA was collected by centrifugation, washed with DI water and ethanol, and dried.

Synthesis of M-PA

2.0 mmol $Zn(OAc)_2 \cdot 2H_2O$ and 0.4 mmol $Co(OAc)_2 \cdot 4H_2O$ (Zn/Co = 5:1) were dispersed into 20 mL of DI water and stirred at room temperature to form mixed solution. Then, 20 mL phytic acid solution ($V_{\text{phytic acid}}$: $V_{\text{DI water}}$ = 1:100) was added to the solution of Zn^{2+}/Co^{2+}. Afterwards, the mixture solution was stirred at room temperature for 30 min. Finally, M-PA was collected by centrifugation, washed with DI water and ethanol, and dried.

Synthesis of Co@NC, $Co_2P_2O_7$@PC and Co_2P@NPC

To prepare Co_2P@NPC, the ZIF-L@M-PA was placed into crucible and heated under Ar atmosphere at 900 °C for 2 h with a heating rate of 5 °C min^{-1}. The Co@NC, $Co_2P_2O_7$@PC were synthesized by using ZIF-L and M-PA layer as precursors under the same calcination conditions with that of Co_2P@NPC.

Synthesis of control samples with different Zn/Co mole ratios and annealing temperatures

Co_2P@NPC with different Zn/Co mole ratios (*i.e.*, NPC-Zn (pure Zn), Co_2P@NPC-1:1 (Zn/Co = 1:1), Co_2P@NPC-1:5 (Zn/Co = 1:5) and Co_2P@NPC-Co (pure Co)) were synthesized under the same conditions as that of Co_2P@NPC, except the mole ratio between Zn and Co. Co_2P@NPC-800 and Co_2P@NPC-1000 were synthesized by annealing ZIF-L@M-PA at 800 and 1000 °C for 2 h, respectively.

Materials characterizations

Powder X-ray diffraction patterns (PXRD) were collected on Bruker D8 Advance ECO X-ray diffractometer with Cu-Kα source (λ = 1.5418 nm) at 40 kV and 25 mA. Fourier transform infrared (FT-IR) spectra were acquired on Bruker Vertex FTIR Spectrometer. Raman spectra were measured on LabRAM HR Evolution with laser excitation of 532 nm. The scanning electron microscope (SEM) was performed on Hitachi SU8230 SEM instruments. X-ray photoelectron spectroscopy (XPS) data were collected on a Escalab 250Xi instrument with Al Kα radiation. The Brunauer-Emmett-Teller (BET) surface area was evaluated by N_2 adsorption-desorption isotherms, which were performed at 77 K using BELSORP-max. Pore size analysis were analyzed by Non-Local Density Functional Theory (NLDFT) method. All samples were degassed at 100 ºC for 20 h before testing. Transmission electron microscopy (TEM) and high-resolution transmission electron

microscope (HRTEM) observations were conducted with a FEI Talos F200X G2 microscope with operating voltage at 200 kV equipped with an energy-dispersive spectrometer detector. The concentrations of Co species for as-prepared catalysts were determined by inductively coupled plasma optical emission spectrometer (ICP-OES) (Agilent 5110).

Electrochemical Measurements

Oxygen evolution reaction (OER) and oxygen reduction reaction (ORR) measurements of as-prepared samples were carried on electrochemical workstation (CHI 760E) with a standard three-electrode system. Carbon rods were used as counter electrodes (CE) for OER and ORR. The electrolyte used for OER was 1.0 M KOH, and the electrolyte used for ORR was 0.1 M KOH. All the potentials were presented versus reversible hydrogen electrode (*vs.* RHE) according to Nernst equation.

OER measurements.

For OER measurements, the catalysts-loaded carbon papers (0.5×2.0 cm^2) were used as the working electrodes, and the area of loading catalyst was controlled to 0.5×1.0 cm^2 (catalyst loading: 1.0 mg cm^{-2}). A Hg/HgO electrode was used as the reference electrode. The catalyst ink was prepared by dispersing 5 mg catalyst in 1 mL solution (500 μL H_2O, 460 μL EtOH and 40 μL nafion) with ultrasonication for 60 min. Then, 100 μL ink was dropped on a piece of carbon paper and dried at room temperature. Linear scan voltammetry (LSV) tests were carried out in 1.0 M KOH solution with a sweep rate of 5 mV s^{-1}, chronopotentiometry tests were performed at the current density of 10 mA cm^{-2}. The electrochemically active surface area (ECSA) was calculated by measuring the double layer capacitance (C_{dl}) under the potential window of 0.944-1.044 V *vs.* RHE with various scan rates (10-90 mV s^{-1}). The electrochemical impedance spectra (EIS) measurements were performed at 1.574 V *vs.* RHE under 5 mV of amplitude from 100 kHz to 0.1 Hz.

TOF calculation

We assumed that all the species of Co are catalytically active and calculated their turnover frequencies (TOFs). Therefore, the values of TOF were further estimated via the following function,[1]

$$\mathrm{TOF} = (j \times A)/(4 \times \mathrm{F} \times n)$$

where j is current density at a given overpotential, A is surface area of electrode, 4 represents 4 e^- $\cdot mol^{-1}$ of O_2, and F is Faraday constant (96485 C mol^{-1}). The value of n can be calculated through the catalyst loading and inductively coupled plasma optical emission spectrometer (ICP-OES) results (Table S1)

ECSA calculation

The electrochemical surface area (ECSA) was estimated by electrochemical double-layer capacitance (C_{dl}) according to the following equation: [2,3]

$$ECSA = C_{dl}/C_s$$

$$j_{ECSA} = j/ECSA$$

where the specific capacitance C_s for a flat surface in an alkaline medium is 40 μF cm^{-2}.

Faradaic efficiency calculation

The Faradic efficiency (f) was determined by a rotating ring-disk electrode (RRDE) consisting of a glassy carbon disk electrode and a Pt ring electrode in N_2-saturated 1.0 M KOH electrolyte with rotating speed of 1600 rpm. Fig. S17a illustrated the working principle of the RRDE in measuring f. The f was calculated by the followed equation:

$$f = I_r/NI_d$$

where I_d and I_r are the disk and ring current, respectively, and N is the ring collection efficiency (N ~ 0.2, calibrated with a potassium ferricyanide redox couple).[4,5]

ORR measurements.

For ORR measurements, glassy carbon electrodes (GC, 5 mm in diameter) were used as the working electrodes and a Ag/AgCl electrode was used as the reference electrode. The catalyst ink was prepared by dispersing 5 mg catalyst in 1 mL solution (500 μL H_2O, 460 μL EtOH and 40 μL nafion) with ultrasonication for 60 min. Then, 20 μL ink was dropped on a mirror-polished GC and dried at room temperature (catalyst loading: 0.5 mg cm^{-2}). For ORR, cyclic voltammetry (CV) measurements were carried out in N_2/O_2 saturated 0.1 M KOH solution with a scan rate of 50 mV s^{-1}, LSV tests were carried out in O_2 saturated 0.1 M KOH solution with a sweep rate of 5 mV s^{-1}, chronoamperometry tests were performed at 0.664 V *vs.* RHE.

Based on the LSV data, the electron transfer numbers (n) was calculated according to the Koutecky-

Levich (K-L) equation:

$$\frac{1}{j} = \frac{1}{j_K} + \frac{1}{j_L} = \frac{1}{j_K} + \frac{1}{0.2nFD_{O2}^{2/3}\omega^{1/2}v^{-1/6}C_{O2}}$$

where j, j_K and j_L are the measured current density, kinetic- and diffusion-limiting current densities, respectively; F is the Faraday constant, D_{O2} is the diffusion coefficient of O_2 in 0.1 M KOH (1.9×10^{-5} cm^2 s^{-1}), ω is the rotation speed in rpm, v is the kinematic viscosity of the electrolyte (1.0×10^{-2} cm^2 s^{-1}), C_{O2} is the bulk concentration of O_2 (1.2×10^{-6} mol cm^{-3}).

Zinc-air battery

Catalyst layer and hydrogel were prepared according to the reported literature.[6] Zn plate was used as the anode. Hydrogel was immersed in 6.0 M KOH and 0.2 M $Zn(OAc)_2$ aqueous solution as electrolyte. The discharge curves were carried on a CHI 760E electrochemical workstation. The galvanostatic discharge-charge cycle stability was tested on a Neware Battery test instrument.

Characterization and Performance Section

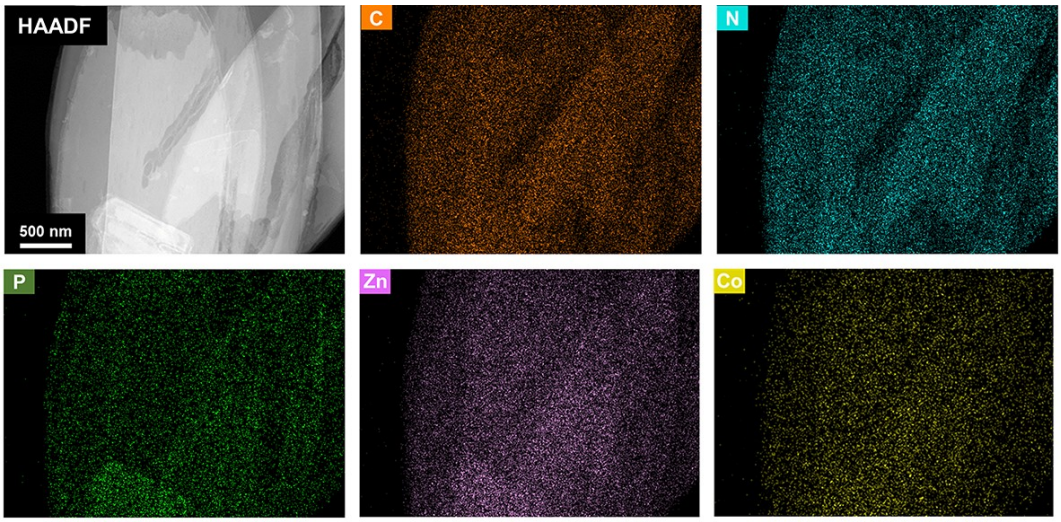

Fig. S1 EDX mappings of ZIF-L@M-PA.

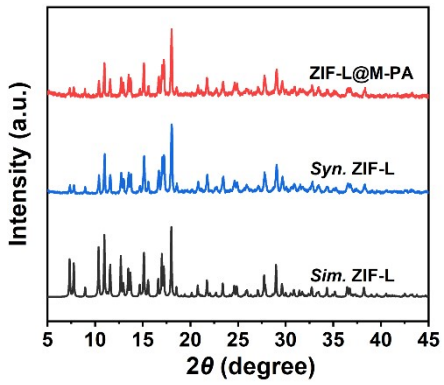

Fig. S2 PXRD patterns of ZIF-L, ZIF-L@M-PA.

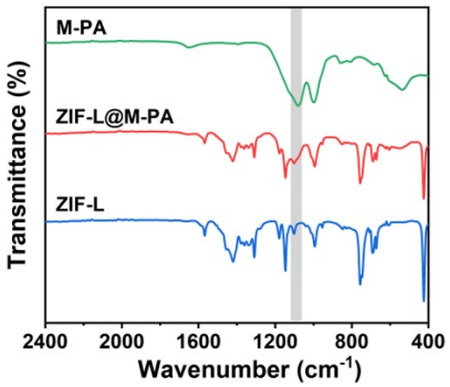

Fig. S3 FT-IR spectra of ZIF-L, ZIF-L@M-PA and M-PA.

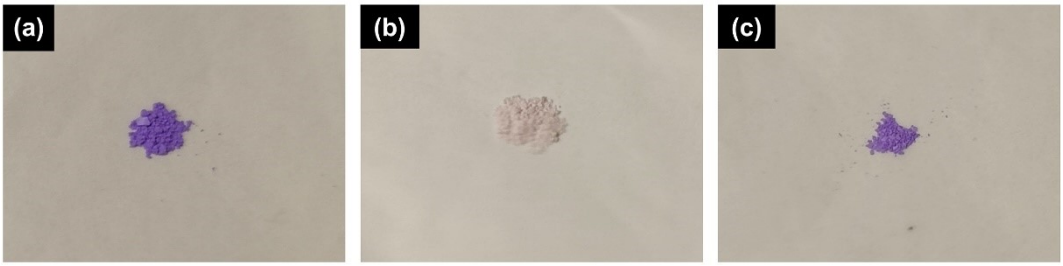

Fig. S4 Digital photographs of (a) ZIF-L, (b) M-PA and (c) ZIF-L@M-PA.

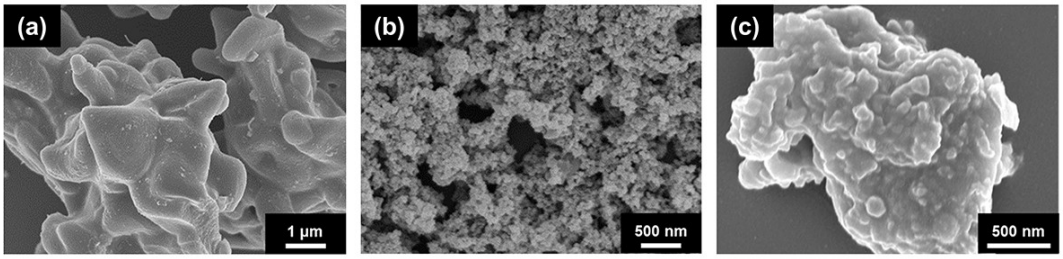

Fig. S5 SEM images of (a) Co@NC, (b) M-PA and (c) $Co_2P_2O_7$@PC.

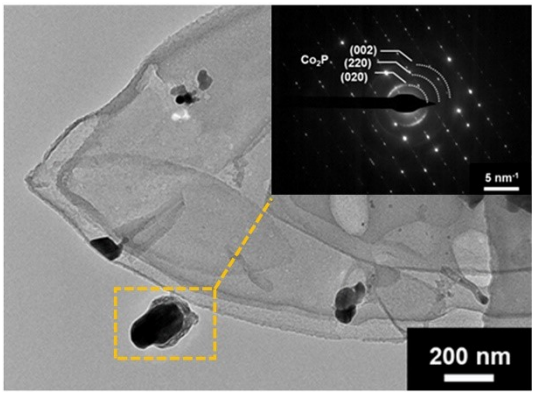

Fig. S6 SAED pattern of Co_2P@NPC.

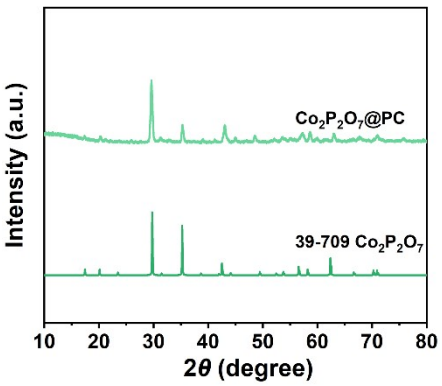

Fig. S7 PXRD pattern of $Co_2P_2O_7$@PC.

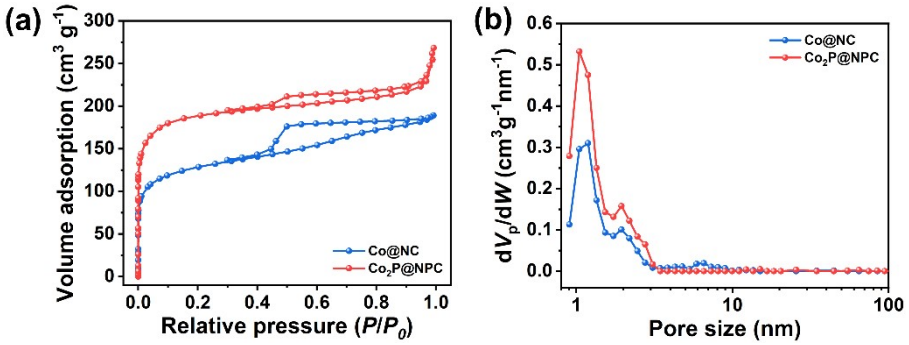

Fig. S8 (a) N_2 adsorption-desorption isotherms and (b) pore size distribution of Co@NC and Co_2P@NPC.

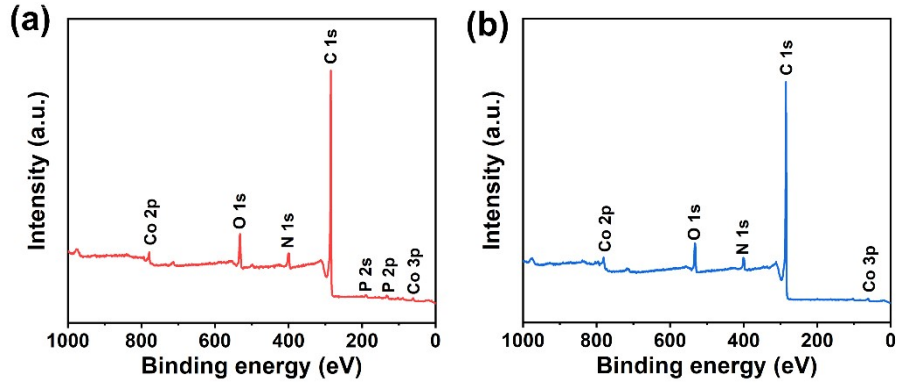

Fig. S9 Full XPS spectra of (a) Co_2P@NPC and (b) Co@NC.

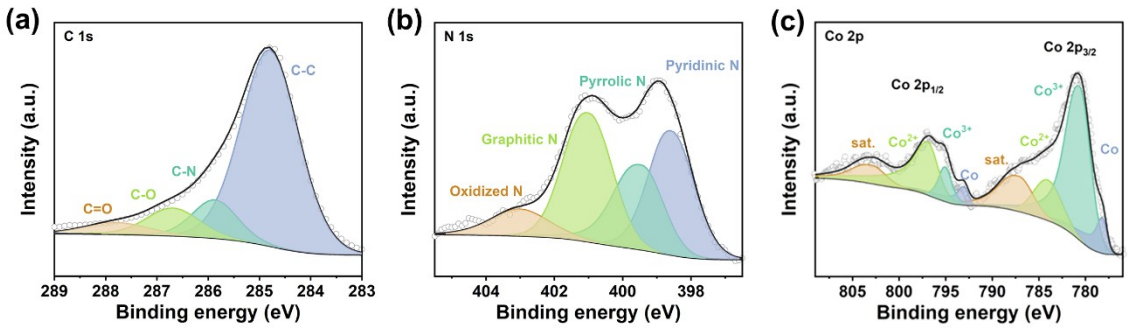

Fig. S10 High-resolution XPS spectra of (a) C 1s, (b) N 1s and (c) Co 2p for Co@NC.

The high-resolution X-ray photoelectron spectroscopy (XPS) spectrum for C 1s in Co@NC exhibited four types of peaks: C-C (284.8 eV), C-N (285.9 eV), C-O (286.7 eV), C=O (287.8 eV) (Fig. S10a). The high-resolution N 1s spectrum presents four forms of N species: pyridinic N (398.6 eV), pyrrolic N (399.5 eV), graphitic N (401.0 eV) and oxidized N (403.0 eV) (Fig. S10b). As depicted in the high-resolution image of the Co 2p region (Fig. S10c), the peaks centered at 780.6 and 795.1 eV were allocated to $2p_{3/2}$ and $2p_{1/2}$ of Co^{3+}, and the peaks at 784.1 and 796.9 eV belonged to $2p_{3/2}$ and $2p_{1/2}$ of Co^{2+}, which was attributed to superficial oxidation of Co species. The peaks at

778.2 and 793.1 eV corresponded to the $2p_{3/2}$ and $2p_{1/2}$ of reduced Co. Moreover, the peak at 787.2 and 803.0 eV were satellite peaks of cobalt.

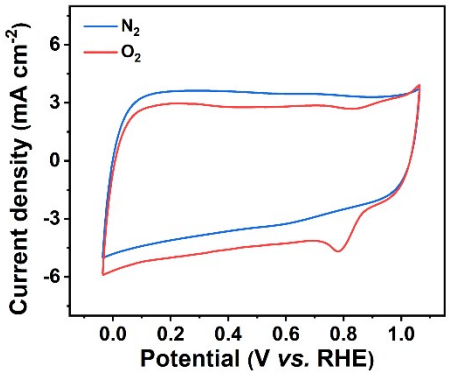

Fig. S11 CV curves of Co_2P@NPC in N_2/O_2-saturated 0.1 M KOH.

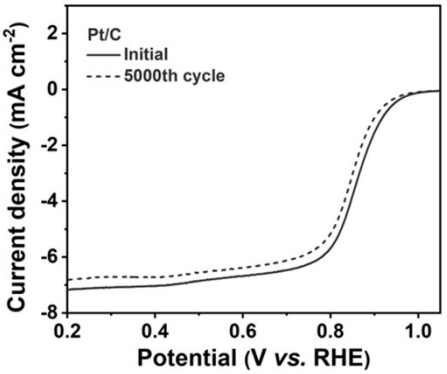

Fig. S12 LSV curves of Pt/C before and after accelerated durability test between 0.6 and 1.0 V *vs.* RHE.

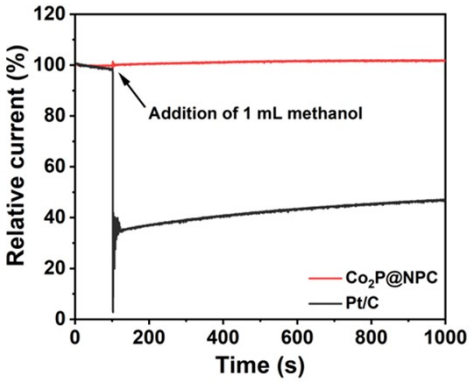

Fig. S13 Chronoamperometric response of Co_2P@NPC at 0.664 V *vs.* RHE after addition of 1 mL methanol into 0.1 M KOH solution.

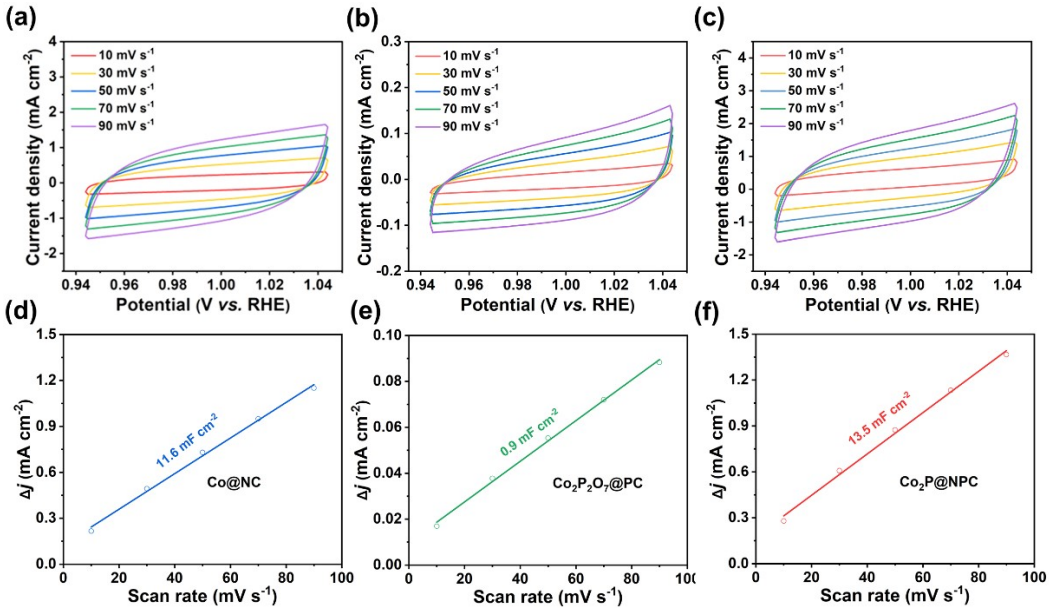

Fig. S14 CV of (a), (d) Co@NC, (b),(e) $Co_2P_2O_7$@PC, (c),(f) Co_2P@NPC at different scan rates under the potential window of 0.944-1.044 V *vs.* RHE and the corresponding C_{dl}.

The ECSA values of Co@NC, $Co_2P_2O_7$@PC and Co_2P@NPC electrocatalysts are 290 cm^2_{ECSA}, 22.5 cm^2_{ECSA} and 337.5 cm^2_{ECSA}, respectively.

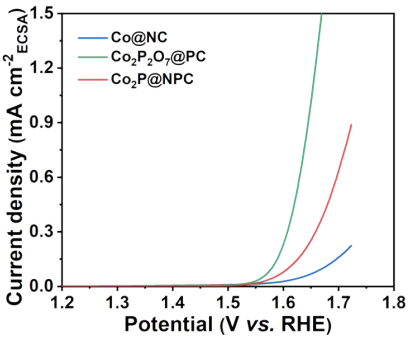

Fig. S15 ECSA-normalized LSV curves of Co@NC, $Co_2P_2O_7$@PC and Co_2P@NPC.

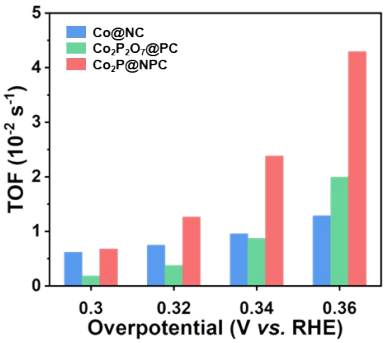

Fig. S16 TOFs of Co@NC, $Co_2P_2O_7$@PC and Co_2P@NPC at different overpotentials.

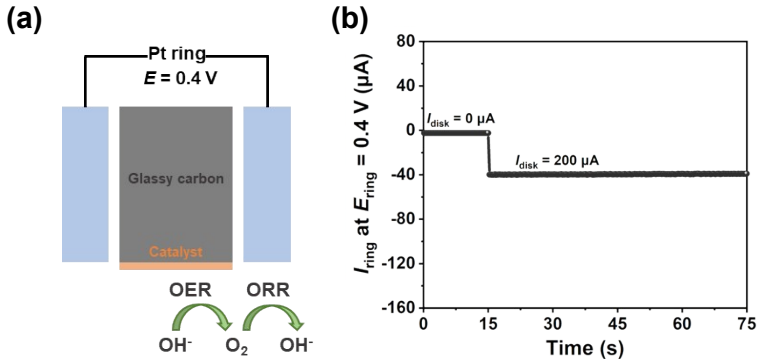

Fig. S17 (a) Schematic illustration of the continuous OER (disk electrode) to ORR (ring electrode) process initiated on a RRDE. (b) Ring current of Co_2P@NPC on an RRDE (1600 rpm) in N_2-saturated 1.0 M KOH solution (ring potential 0.40 V).

When a constant current (I_d = 200 μA) was applied to the disk electrode for O_2 generation, a ring current of ~39.8 μA from O_2 reduction was detected. The *f* of Co_2P@NPC was determined to be ~ 99.5%.

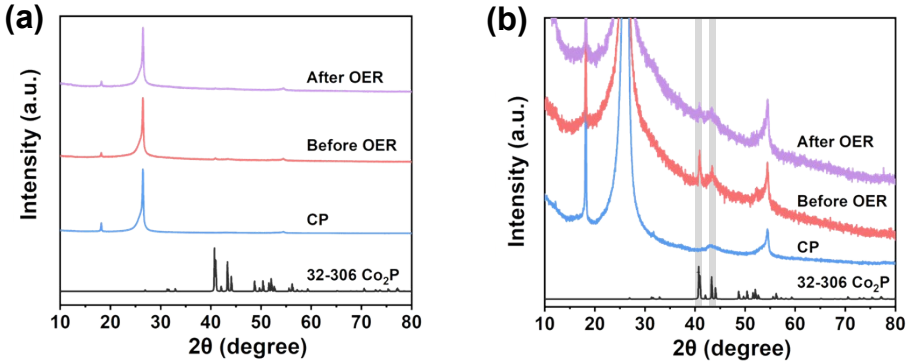

Fig. S18 (a) PXRD patterns of Co_2P@NPC before and after OER test, (b) the corresponding enlarged patterns.

In the present work, the catalysts-loaded carbon paper (CP) was used as the working electrode. Therefore, the PXRD patterns of Co_2P@NPC before and after chronopotentiometry test were collected directly on CP, and the obtained SEM images derived from the samples peeled off from CP. As shown in Fig. S18a, the PXRD patterns mainly presented the characteristic peaks of CP due to the low loading of Co_2P@NPC on CP. However, with the enlargement of peaks intensity, the consistent peaks assigned to Co_2P (JCPDS#32-306) were observed on Co_2P@NPC before and after OER test (Fig. S18b). Meanwhile, the peaks of Co_2P@NPC after OER test became weaker, which

may result from the formation of amorphous cobalt oxo-/hydroxide layer over the surface of Co_2P nanoparticles during the OER process[7,8]. Further, SEM test was carried out to verify the morphology change of Co_2P@NPC after OER test. As displayed in Fig. S19, Co_2P@NPC basically maintained the leaf-like shape after 24 h chronopotentiometry test. The agglomeration phenomenon may due to the introduction of nafion binders during the electrode preparation process.

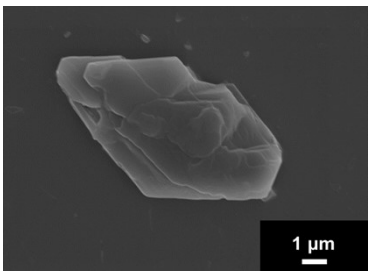

Fig. S19 SEM image of Co_2P@NPC after OER test.

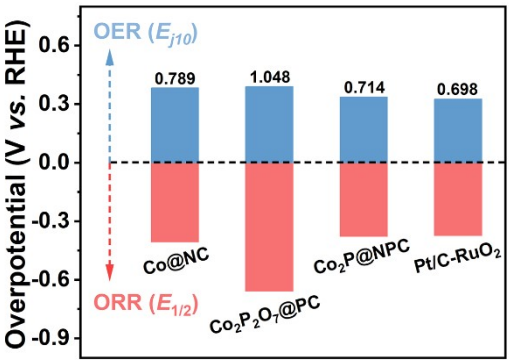

Fig. S20 Comparison of bifunctional activity between Co_2P@NPC and other control samples.

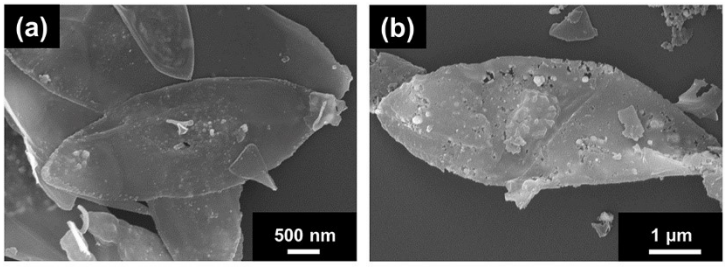

Fig. S21 SEM images of (a) Co_2P@NPC-800 and (b) Co_2P@NPC-1000.

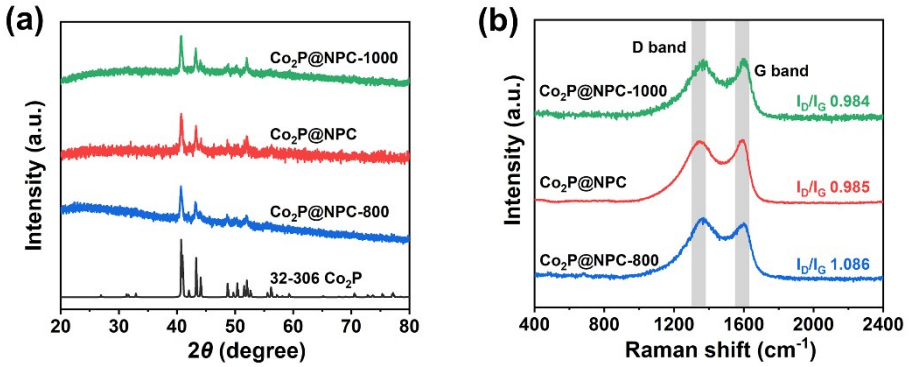

Fig. S22 (a) PXRD patterns and (b) Raman spectra of Co_2P@NPC annealed at different temperatures.

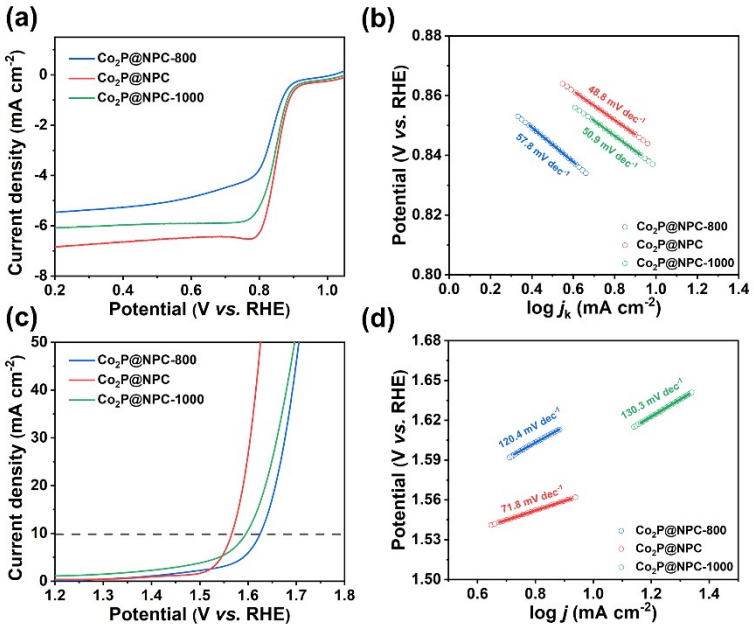

Fig. S23 (a) ORR polarization curves and (b) Tafel slopes of Co_2P@NPC carbonized at different temperatures. (c) OER polarization curves and (d) Tafel slopes of Co_2P@NPC carbonized at different temperatures.

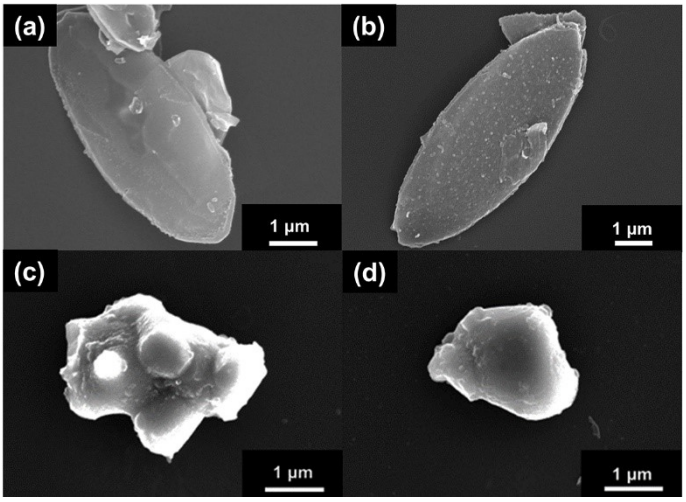

Fig. S24 SEM images of Co_2P@NPC derived from ZIF-L with different Zn/Co mole ratios: (a) NPC-Zn, (b) Co_2P@NPC-1:1, (c) Co_2P@NPC-1:5 and (d) Co_2P@NPC-Co.

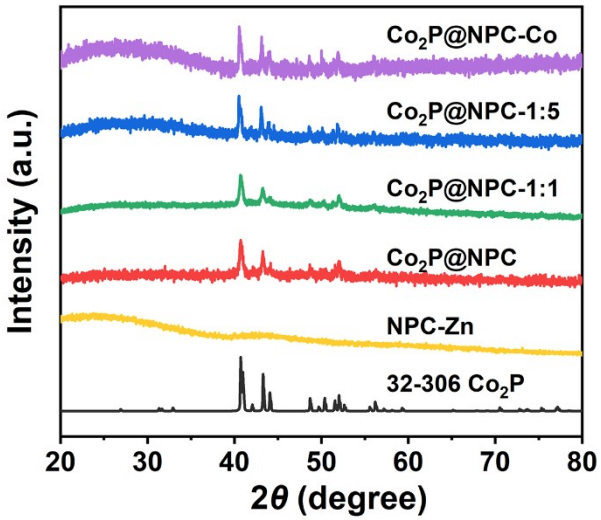

Fig. S25 PXRD patterns of Co_2P@NPC derived from ZIF-L with different Zn/Co mole ratios.

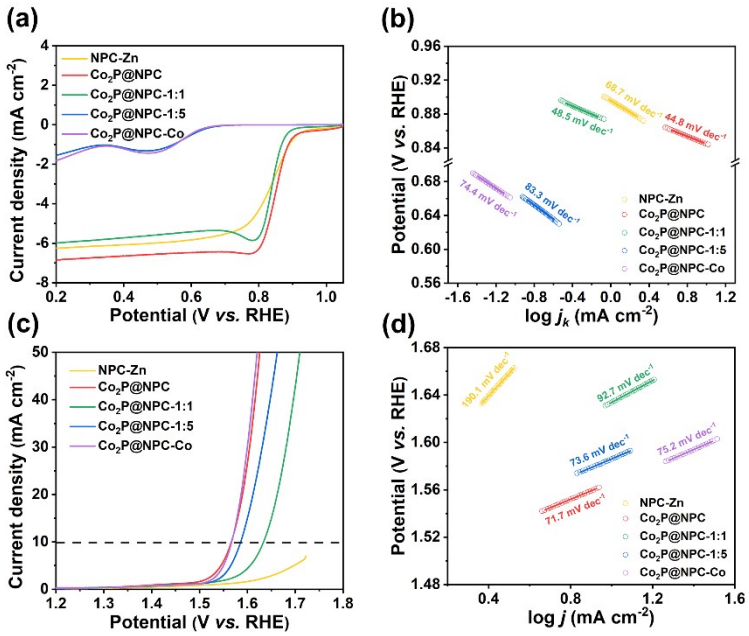

Fig. S26 (a) ORR polarization curves and (b) Tafel slopes of Co_2P@NPC derived from ZIF-L with different Zn/Co mole ratios. (c) OER polarization curves and (d) Tafel slopes of Co_2P@NPC derived from ZIF-L with different Zn/Co mole ratios.

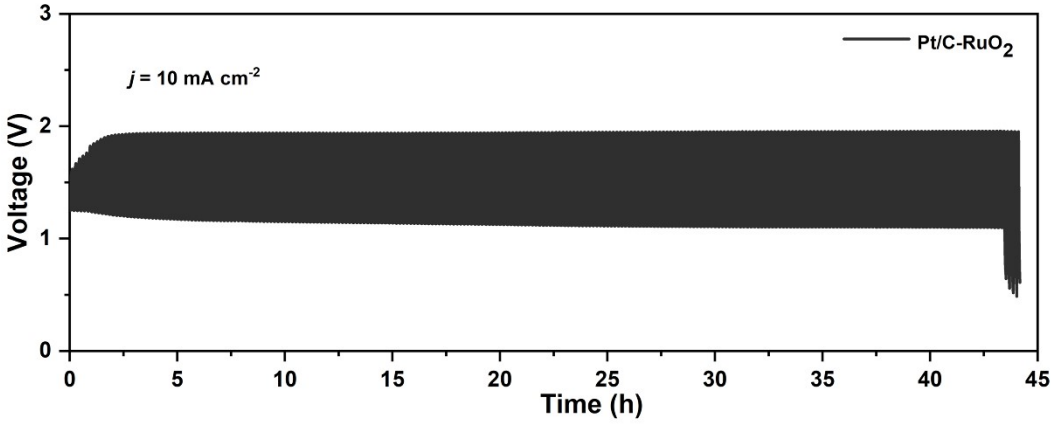

Fig. S27 Discharge-charge cycling curve of Pt/C-RuO_2.

Table S1 ICP-OES data of Co@NC, $Co_2P_2O_7$@PC and Co_2P@NPC.

Catalysts	Co Content (*wt*%)
Co@NC	8.0653
$Co_2P_2O_7$@PC	2.6932
Co_2P@NPC	7.1653

Table S2 Comparison of the as-prepared Co_2P@NPC with other MOF-derived bifunctional oxygen reaction catalysts.

Catalysts	ORR		OER		ΔE (V)	Peak power density (mW cm^{-2})	References
	Loading (mg cm^{-2})	$E_{1/2}$ (V)	Loading (mg cm^{-2})	η@10 (mV)			
Co_2P@NPC	0.5	0.852	1	336	0.714	198.14	This work
CoFeN-NCNTs//CCM	0.26	0.840	0.28	325	0.715	145.00	S1[9]
CoNi/Co-N@HNC	0.25	0.860	0.25	350	0.720	179.10	S2[10]
Fe/Co/Zn-CNZIF	/	0.853	/	352	0.729	156.70	S3[11]
ZnNi-DCN-1000	/	0.820	/	330	0.740	298.90	S4[12]
H-NSC@Co/NSC	0.3	0.850	0.3	370	0.750	286.70	S5[13]
CoNi-CoO-NiO@NC-800	0.5	0.830	0.5	352	0.752	223.00	S6[14]
Fe-Co-Ni MOF	0.28	0.730	0.28	254	0.754	161.00	S7[15]
Co_3O_4@ND-CN	0.51	0.81	0.51	336	0.756	105.00	S8[16]
Co_9S_8-FeS_2@N-CNFs	/	0.800	/	330	0.760	214.00	S9[17]
FeS_2-CoS_2/NCFs	0.23	0.810	0.23	340	0.760	257.00	S10[18]
Co@CNT-NC	0.5	0.870	0.5	403	0.763	179.30	S11[19]
CuCo-N_x@N-CCs	0.26	0.800	0.26	350	0.780	86.5	S12[20]
$FeCoO_x$@NG	1	0.790	1	340	0.780	215	S13[21]
NiCo-NC	0.4	0.856	0.28	406	0.780	163.70	S14[22]
Co_7Fe_3/CFNC	0.3	0.845	0.3	402	0.787	103.00	S15[23]
Ox-MnCoNi-C (4 h)	0.2	0.800	0.2	360	0.790	125.00	S16[24]
$NiFe_3$@NGHS-NCNTs	0.2	0.823	0.2	383	0.790	102.82	S17[25]
ZnCo-NCNT/Mo_2C-800	0.4	0.821	0.4	382	0.791	231.60	S18[26]
NiY/C@Co/C	0.2	0.830	0.2	392	0.792	102.20	S19[27]
Fe-Co/Co_3O_4@NC-900	0.26	0.840	1	410	0.800	107.6	S20[28]
Co/CeO_2-NCNA@CC	/	0.770	/	350	0.810	123.00	S21[29]
Co/CNWs/CNFs	0.51	0.820	0.51	412	0.822	304	S22[30]
Mn/Co-450	0.25	0.780	0.25	380	0.830	115.50	S23[31]

Supplementary References

1. G. Zhang, G. Wang, Y. Liu, H. Liu, J. Qu and J. Li, *J Am Chem Soc*, 2016, **138**, 14686-14693.
2. T. Xiong, Z. Zhu, Y. He, M. S. Balogun and Y. Huang, *Small Methods*, 2023, **7**, e2201472.
3. P. Zhang, X. F. Lu, J. Nai, S. Q. Zang and X. W. D. Lou, *Adv. Sci.*, 2019, **6**, 1900576.
4. H. Fei, J. Dong, Y. Feng, C. S. Allen, C. Wan, B. Volosskiy, M. Li, Z. Zhao, Y. Wang, H. Sun, P. An, W. Chen, Z. Guo, C. Lee, D. Chen, I. Shakir, M. Liu, T. Hu, Y. Li, A. I. Kirkland, X. Duan and Y. Huang, *Nat. Catal.*, 2018, **1**, 63-72.
5. F. Li, Y. Li, L. Li, W. Luo, Z. Lu, X. Zhang and Z. Zheng, *Chem. Sci.*, 2022, **13**, 9256-9264.
6. Q. Wang, Q. Feng, Y. Lei, S. Tang, L. Xu, Y. Xiong, G. Fang, Y. Wang, P. Yang, J. Liu, W. Liu and X. Xiong, *Nat. Commun.*, 2022, **13**, 3689.
7. K. Xu, H. Cheng, L. Liu, H. Lv, X. Wu, C. Wu and Y. Xie, *Nano Lett.*, 2017, **17**, 578-583.
8. Z. Pu, T. Liu, I. S. Amiinu, R. Cheng, P. Wang, C. Zhang, P. Ji, W. Hu, J. Liu and S. Mu, *Adv. Funct. Mater.*, 2020, **30**, 2004009.
9. G. Zhou, G. Liu, X. Liu, Q. Yu, H. Mao, Z. Xiao and L. Wang, *Adv. Funct. Mater.*, 2021, **32**, 2107608.
10. Y. Tan, Z. Zhang, Z. Lei, L. Yu, W. Wu, Z. Wang and N. Cheng, *Appl. Catal., B*, 2022, **304**, 121006.
11. Z. Guo, Y. Ma, Y. Zhao, Y. Song, S. Tang, Q. Wang and W. Li, *J. Power Sources*, 2022, **542**, 231723.
12. B. Wulan, X. Cao, D. Tan, X. Shu and J. Zhang, *Adv. Funct. Mater.*, 2022, **32**, 2203842.
13. W. Li, J. Wang, J. Chen, K. Chen, Z. Wen and A. Huang, *Small*, 2022, **18**, e2202018.
14. X. Duan, S. Ren, F. Ge, X. Zhu, M. Zhang and H. Zheng, *Nanoscale*, 2021, **13**, 17655-17662.
15. F. Shahbazi Farahani, M. S. Rahmanifar, A. Noori, M. F. El-Kady, N. Hassani, M. Neek-Amal, R. B. Kaner and M. F. Mousavi, *J. Am. Chem. Soc.*, 2022, **144**, 3411-3428.
16. W. Tang, K. Teng, W. Guo, F. Gu, B. Li, R. Qi, R. Liu, Y. Lin, M. Wu and Y. Chen, *Small*, 2022, **18**, e2202194.
17. L. Sun, S. Huang, X. Zhao, L. Li, X. Zhao and W. Zhang, *Langmuir*, 2022, **38**, 11753-11763.
18. X. Shi, B. He, L. Zhao, Y. Gong, R. Wang and H. Wang, *J. Power Sources*, 2021, **482**, 228955.
19. B. Gao, M. Tan, W. Xi, X. Lin, Z. Li, M. Shen and B. Lin, *J. Power Sources*, 2022, **527**, 231205.
20. Y. Xie, C. Feng, Y. Guo, A. Hassan, S. Li, Y. Zhang and J. Wang, *J. Power Sources*, 2022, **517**, 230721.
21. Z. Zheng, C. Wang, P. Mao, Y. Zhu, R. Ran, W. Zhou, K. Liao and Z. Shao, *Carbon Energy*, 2022, DOI: 10.1002/cey2.274.
22. F. Wang, Y. Xu, Y. Wang, Z. Liang, R. Zhang, Y. Wang, H. Zhang, W. Zhang, R. Cao and H. Zheng, *Chem. Commun.*, 2021, **57**, 8190-8193.
23. T.-x. Tu, X. Zhou, P.-f. Zhang, L. Tan, Z.-f. Xu, M.-q. Liu, W.-y. Li, X.-m. Kang, Y.-j. Wu and J.-z. Zheng, *ACS Sustainable Chem. Eng.*, 2022, **10**, 8694-8703.

24. C. Rui, T. Zhang, Y. Jiang, D. Xie, M. Li, Q. Lu and Y. Bu, *Energy Fuels*, 2022, **36**, 12816-12825.
25. Y. Ma, W. Chen, Z. Jiang, X. Tian, X. WangGuo, G. Chen and Z.-J. Jiang, *J. Mater. Chem. A*, 2022, **10**, 12616-12631.
26. F. Li, J. Niu, Y. Liu, T. Qin, D. Zhao, Q. Zhao and X. Liu, *J. Power Sources*, 2023, **553**, 232310.
27. F. Liu, H. Peng, Y. Kang, Y. Hao, L. Li, H. Xin, H. Kang, W. Wang and Z. Lei, *ACS Sustainable Chem. Eng.*, 2022, **10**, 10978-10988.
28. Q.-H. Kong, X.-W. Lv, C.-C. Weng, J.-T. Ren, W.-W. Tian and Z.-Y. Yuan, *ACS Sustainable Chem. Eng.*, 2022, **10**, 11441-11450.
29. S. Li, H. Zhang, L. Wu, H. Zhao, L. Li, C. Sun and B. An, *J. Mater. Chem. A*, 2022, **10**, 9858-9868.
30. C. Xia, L. Huang, D. Yan, A. I. Douka, W. Guo, K. Qi and B. Y. Xia, *Adv. Funct. Mater.*, 2021, **31**, 2105021.
31. C. Huang, Y. Zhang, X. Li, H. Cao, Y. Guo and C. Zhang, *Appl. Catal., B*, 2022, **319**, 121909.